Investigation of coherent Fourier scatterometry as a calibration tool for determination of steep side wall angle and height of a nanostructure

Paul, A.; Rafigh Doost, J.; Dou, X.; Pereira, S.F.

DOI
10.1088/1361-6501/ad3773

Publication date
2024

Document Version
Final published version

Published in
Measurement Science and Technology

Citation (APA)
Paul, A., Rafigh Doost, J., Dou, X., & Pereira, S. F. (2024). Investigation of coherent Fourier scatterometry as a calibration tool for determination of steep side wall angle and height of a nanostructure. *Measurement Science and Technology*, *35*(7), Article 075202. https://doi.org/10.1088/1361-6501/ad3773

Measurement Science and Technology

PAPER • OPEN ACCESS

Investigation of coherent Fourier scatterometry as a calibration tool for determination of steep side wall angle and height of a nanostructure

To cite this article: Anubhav Paul *et al* 2024 *Meas. Sci. Technol.* **35** 075202

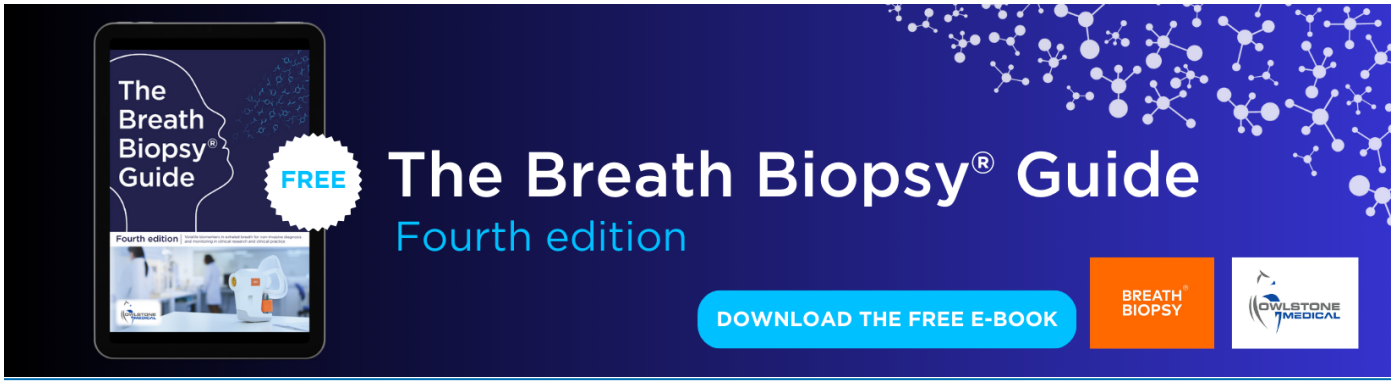

OPEN ACCESS
IOP Publishing
Measurement Science and Technology
Meas. Sci. Technol. **35** (2024) 075202 (11pp)
https://doi.org/10.1088/1361-6501/ad3773

Investigation of coherent Fourier scatterometry as a calibration tool for determination of steep side wall angle and height of a nanostructure

Anubhav Paul*, Jila Rafighdoost, Xiujie Dou and Silvania F Pereira

Imaging Physics Department, Faculty of Applied Sciences, Delft University of Technology, Lorentzweg 1, 2628 CJ Delft, The Netherlands

E-mail: A.Paul-1@tudelft.nl

Received 27 November 2023, revised 20 March 2024
Accepted for publication 25 March 2024
Published 2 April 2024

Abstract

Nanostructures with steep side wall angles (swa) play a pivotal role in various technological applications. Accurate characterization of these nanostructures is crucial for optimizing their performance. In this study, we propose a far-field detection method based on coherent Fourier scatterometry (CFS) for accurate quantification of steep swa and heights in cliff-like nanostructures. Our approach introduces a parameter termed 'visibility', derived from the unique far-field signatures of cliff-like nanostructures. This parameter serves as a quantitative metric for the calibration of swa and heights. The heightened sensitivity of our method is demonstrated, particularly when the incident polarization is perpendicular to the invariant direction of the nanostructure for swa calibration, while both polarization states exhibit sensitivity to height calibration. Furthermore, a comprehensive sensitivity analysis reveals the stable nature of our method, showcasing that even with fluctuations of ± 10 nm in the position of the nanostructure, the resulting swa remains stable within a range of $\pm 0.5°$. The exponential variation of the visibility parameter with edge roundness is observed, with fluctuations in edge roundness within 10 nm resulting in swa variations within 1.7° for both polarization states. In experimental validations, our results demonstrate reasonable agreement between CFS-derived and AFM measurements. The AFM data for swa ($77.99° \pm 1.37°$) and height (148.35 nm ± 2.11 nm) are corroborated with CFS-derived value of swa ($77.75° \pm 3.61°$, $78.36° \pm 3.89°$) and height (149.42 nm ± 1.66 nm, 150.05 nm ± 1.04 nm) obtained from calibration curves for TM and TE incident beams, respectively. Overall, our findings underscore CFS as a potential and reliable tool for nanostructure characterization, offering precise measurements that are pivotal for advancing nanotechnology.

Keywords: steep side wall angle, coherent Fourier scatterometry, calibration

* Author to whom any correspondence should be addressed.

1. Introduction

In the ever-evolving realm of nanotechnology, the production of nanostructures with precise height and steep side wall angles (swa) stands as a pursuit of paramount importance [1, 2]. These sharply defined structures play a crucial role in the development of cutting-edge semiconductor devices, their dimensions often shrinking to the nanometer scale. Precision at this scale is no longer an aspirational goal; it has become an absolute necessity [3]. Among the myriad of critical parameters, the height and steep swa emerge as a linchpin, particularly in lithography mask fabrication [4, 5]. The height and steep swa hold the key to preventing shadowing effects during the etching process, ensuring that the resulting pattern on the wafer aligns precisely with the design specifications. Even the slightest deviation in the height and swa, especially when dealing with structures at the nanoscale, can trigger a domino effect of consequences, potentially culminating in the failure of the entire semiconductor chip [6]. Thus, the measurement of these steep swa carries tremendous significance, representing both the cornerstone of nanoscale precision and the foundation of faultless device functionality. However, the task of accurately measuring these angles presents a formidable challenge, one that has confounded researchers for years.

While there have been extensive numerical studies focused on accurately measuring both height and steep swa, a method that achieves precise measurements in both aspects remains elusive. Prior endeavors predominantly leaned on simulations and theoretical models, which offered valuable insights [7–10]. However, the practical measurements of these structural parameters remain a formidable task. This disparity between theoretical understanding and practical application has become a pivotal challenge in the realm of nanoscale metrology. Closing this gap is crucial for advancing the field.

In the pursuit of height and swa measurement, several techniques, including scanning electron microscopy (SEM) [11–13], atomic force microscopy (AFM) [14–18], and optical microscopy [19–22], have played pivotal roles. However, each of these approaches brings its own set of drawbacks to the table. SEM, despite its flexibility, grapples with the potential for sample damage, especially when investigating sensitive nanostructures. AFM, on the other hand, faces challenges when dealing with swa greater than the slant angle of its probe tips, limiting its applicability. Although conventional optical microscopy offers non-invasive capabilities and can be utilized in in-line mode, they are constrained by Abbe's diffraction limit and exhibit relatively low spatial resolution [23]. In response to these challenges, scatterometry-based metrology techniques have emerged as a promising alternative [24, 25]. Scatterometry, rooted in the analysis of scattered light, encompasses various modalities, including spectroscopic ellipsometry (SE) [26], Mueller-matrix Fourier scatterometry (MMFS) [27], white light interference Fourier scatterometry (WL-IFS) [28], and critical dimension small angle x-ray scattering (CD-SAXS) [29], offering unique capabilities for nanostructure characterization. All these modalities come with their advantages and disadvantages. SE provides detailed information about thin film properties, including thickness and refractive index. However, it is limited by its sensitivity to surface roughness and the complexity of data analysis. MMFS enables the characterization of complex periodic nanostructures. Yet, its application is often restricted to periodic structures, and it requires advanced modeling for interpretation. WL-IFS excels in height measurements, especially for structures with varying heights. However, it may face challenges in the presence of strong reflections and is confined to the coherence length of the light source. CD-SAXS is a powerful technique for characterizing nanostructures, but it is limited by the brightness of available compact x-ray sources, which leads to long measurement times. Further, these techniques are model-dependent, relying on solving an inverse problem to deduce the values of parameters in the nanostructure, and are mostly applied to periodic structures. Due to the complexity and ill-posed nature of solving the inverse problem for an aperiodic structure like a cliff-like nanostructure, these techniques have commonly been used for characterizing periodic structures. In contrast, coherent Fourier scatterometry (CFS) stands out for its versatility, as it is not confined to periodic problems. CFS can be used as a direct measurement-based technique eliminating the need for modelling in detecting subwavelength isolated particles or subtle alterations in the parameters of nanostructures [30, 31], and a traditional model-based technique for the characterization of periodic nanostructures [32–34]. Notably, recent advancements have seen CFS successfully modeling and experimentally detecting an isolated defect in the periodic nanostructure [35]. However, compared to other techniques CFS is very sensitive to the alignment and stability of the system, and is limited by the surface roughness of the substrate and the noise of the camera pixels [36].

In this article, we propose a metric-driven calibration approach for the characterization of nanostructure geometrical parameters, focusing on aperiodic structures with cliff-like features. Here we depart from traditional inverse problem-fitting methods, which are often challenging for aperiodic structures. Instead, we propose an alternative approach using a quantitative metric termed 'visibility'. This metric is linked to the far-field signatures of the nanostructure, providing a unique means for calibration. Unlike conventional fitting, our methodology associates geometric parameters with the variation of this metric, establishing calibration curves that offer a unique perspective on nanostructure characterization. Through sensitivity analysis, we also evaluate the method's robustness against structural and alignment variations. We further show experimental validation of these calibration curves using CFS. By employing CFS, we perform the height and swa measurements but also establish a comparison with AFM measurements, serving as the ground truth. While our methodology exhibits promise, there are some limitations. Notably, the sensitivity of our approach to noise and the experimental conditions like stability, noise, and alignment of the system will impact the overall accuracy. Further low scattering structures like phase-step objects will be challenging to measure accurately as the noises will dominate the scattering from these objects. Despite these limitations, the successful integration of numerical simulations with experimental validation

substantiates the efficacy of our approach, marking a significant step forward in nanostructure calibration methodologies.

2. Method

2.1. Theory

In this section, we provide a detailed description of the nanostructure under investigation and the associated diffraction theory. The nanostructure in consideration consists of a cliff-like configuration with well-defined swa and height. In figure 1(a) a 2D representation of the nanostructure is schematically shown. The nanostructure is fully characterized by the geometrical parameters: swa and height (h). We introduce an additional parameter b which denotes the projection of the cliff on the $x-$axis, with $b=0$ implying that the nanostructure has swa $=90°$. We define a coordinate system (x,y,z) to describe the geometry of the nanostructure, with the nanostructure being infinite along the $x-$axis and invariant along the $y-$axis. Now the profile of the nanostructure can be expressed as

$$z(x)=\begin{cases} -h & \text{if } x\leqslant -b \\ x\tan(\text{swa})-\frac{h}{2} & \text{if } |x|<b \\ 0 & \text{if } x\geqslant +b. \end{cases} \tag{1}$$

The nanostructure described above can be assumed to act as a pure phase object i.e. a phase step if the slope of the cliff is steep enough [9]. When the phase step interacts with an illuminating focused beam, as shown in figure 1(b), the beam will encounter different path differences across the cliff, and the resulting scattered beam will experience different offsets depending on the reflection function of the nanostructure. For our nanostructure, the reflection function can be expressed as

$$r_{\text{f}}(x)=r\begin{cases} \exp(-2ikh) & \text{if } x\leqslant -b \\ \exp\left[2ik\left(x\tan(\text{swa})-\frac{h}{2}\right)\right] & \text{if } |x|<b \\ 1 & \text{if } x\geqslant +b \end{cases} \tag{2}$$

where k is the wave vector and r(with $|r|\leqslant 1$) is the Fresnel reflection coefficient of the nanostructure. In the angular spectrum decomposition formalism, a focused beam can be decomposed into an infinite number of plane waves of different propagation directions [37]. Let us consider a plane wave (defined by U_i,θ_i,ϕ_i) incident on the nanostructure. The nanostructure (defined by r_{f}) scatters the incident plane wave, which is captured by a microscope objective (O) having numerical aperture (NA), which further propagates it to the back focal plane (BFP) (having coordinate system (ξ,η)) based on the Fourier optics theory [38]. The scattered field propagated to the BFP is given by

$$U_s(\xi,\eta)=\sqrt{\frac{1}{\lambda f}}\exp(2ikf)\int_{-\infty}^{\infty}U_i(x,y)\,r_{\text{f}}(x) \times\exp\left[-2\pi i\left(\frac{\xi}{\lambda f}x+\frac{\eta}{\lambda f}y\right)\right]\mathrm{d}x\,\mathrm{d}y \tag{3}$$

where f is the focal length of the O, and λ is the wavelength of the incident plane wave. Now, if we take into account the scattering from the nanostructure for all plane waves of different propagation directions, each θ_i and ϕ_i will correspond to a distinct point in the BFP. However, it is important to note that this mapping is constrained by the NA of the O.

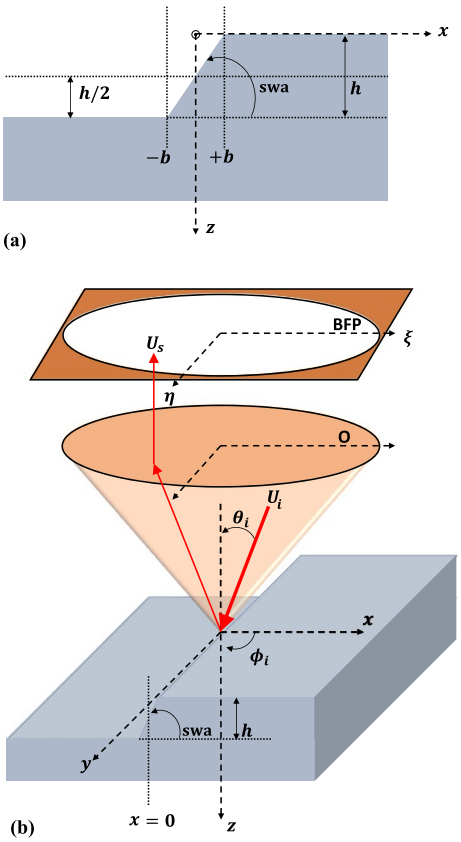

Figure 1. (a) Geometrical representation of the cliff-like nanostructure under investigation. (b) Schematic representation of the cliff-like nanostructure, scattering an incident beam (U_i). The scattered beam (U_s) is captured by a microscope objective (O) having numerical aperture (NA) and propagated to the back focal plane (BFP).

2.2. Experimental setup

In this section, we illustrate the experimental setup of CFS. Its general schematic is shown in figure 2. To begin, a collimated He–Ne laser with a wavelength of $\lambda=633$ nm is utilized for illumination. The collimated laser beam first passes through a linear polarizer (P1). The linearly polarized beam passes through a non-polarizing beam splitter (BS), and then it is directed towards a microscope objective (O) with an NA of 0.4. The O focuses the beam onto the cliff-like nanostructure sample (S). The sample is positioned on a piezo-controlled translation stage (X-Y TS), which is controlled to localize the region of interest in the S and allows for precise observation. The scattered light from the S is collected and directed back through the O and again passes through the BS. We further incorporate a telescopic setup comprising two lenses (L1 and L2) to de-magnify the Fourier plane of the O, directing the light towards a charge-coupled device (CCD) camera. We can choose the output polarization at the CCD with the help of a

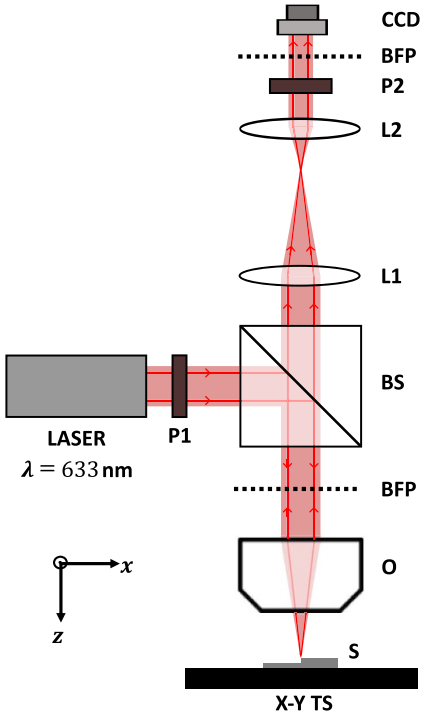

Figure 2. Schematic of the experimental setup of coherent Fourier scatterometry (CFS).

second linear polarizer (P2). This approach enables the simultaneous detection of the angular spectrum for all scattered waves from every incident plane wave within the focused spot.

With the help of P1 and P2, we can choose between two orthogonal configurations of polarization, TE and TM. We use these two polarization configurations throughout all experiments and simulations in this work. Here, TE polarization means that the polarization direction of P1 at the pupil is parallel to the invariant direction of the structure (i.e. $y-$axis). Consequently, TM polarization means that the polarization direction of P1 at the pupil is perpendicular to the invariant direction of the structure (i.e. $y-$axis). P2 is always aligned parallel to P1.

2.3. Numerical model

The intricate electromagnetic interaction between a focused beam and a nanostructure characterized by steep swa presents a formidable challenge. To tackle this complex problem, we employed rigorous 3D electromagnetic simulations, specifically the finite difference time domain (3D-FDTD) method, employing a commercial software package (Lumerical FDTD) [39]. Within the FDTD framework, Maxwell's equations are solved on discretized Yee grids (i.e. spatial and temporal grids) in the time domain.

In our simulations, we replicate the experimental conditions by modeling a cliff-like nanostructure invariant along one direction (along $y-$axis) and profile variation along the orthogonal direction (along $x-$axis), as the simulation object. The dimension of the simulation domain is chosen to ensure that the width of the focused beam (FWHM ~ 818 nm) remains significantly smaller than the dimension of the simulation

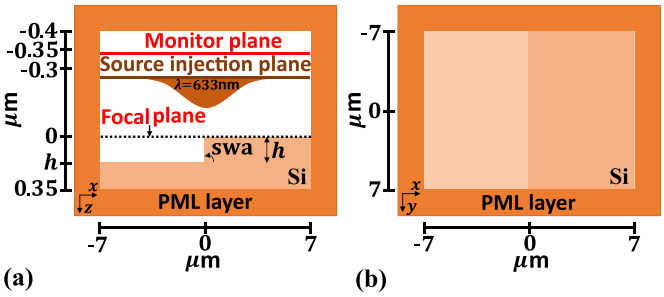

Figure 3. The 3D-FDTD simulation scheme of a cliff-like nanostructure characterized by geometrical parameters: swa and h, being illuminated by a TE or TM polarized focused spot of wavelength 633 nm. The corresponding $y = 0$ plane in (a). The corresponding $z = 0$ plane in (b).

domain ($= 14\,\mu$m). Perfectly matched layer boundary conditions are applied to all boundaries to prevent reflections. For the illumination scheme, we used the vectorial diffraction theory of Richards and Wolf [40, 41] to employ a TE polarized (i.e. the polarization direction at the pupil is parallel to the invariant direction of the nanostructure) or TM polarized (i.e. the polarization direction at the pupil is perpendicular to the invariant direction of the nanostructure) plane wave of wavelength $\lambda = 633$ nm being focused by a microscope objective of numerical aperture 0.4 onto the focal plane (we choose our focal plane to be at the top layer of the cliff-like nanostructure). The scattered near field emanating from the simulation object is computed and sampled at the monitor plane, thereafter propagating it into the far-field through the FDTD simulation.

In figure 3(a), the $y = 0$ plane, and in figure 3(b), the $z = 0$ plane of the complete 3D-FDTD model is depicted. The simulation object's geometry is characterized by the geometrical parameters, swa and height (h). The nanostructure's material is silicon (Si) with a refractive index of $n = 3.88126 + 0.01894i$. To investigate the impact of varying the geometrical parameters of the cliff-like nanostructure on the far-field signatures, we systematically sweep swa (ranging from 70° to 100°) and h (ranging from 100 to 300 nm), while keeping the position of the source injection plane, monitor plane, and computational domain constant.

2.4. Sample preparation

The sample has been fabricated at the TU Delft clean room and it consists of a 2×2 mm square etched on a silicon wafer.

3. Results

3.1. Far-field intensity pattern and definition of visibility

In this section, we perform numerical investigations to understand the electromagnetic interaction of a cliff-shaped nanostructure with that of a linearly polarized focused beam, with the nanostructure being defined by the parameters: swa and h. To understand this phenomenon, let us consider one such nanostructure with parameters: swa $= 90°$ and $h = 150$ nm.

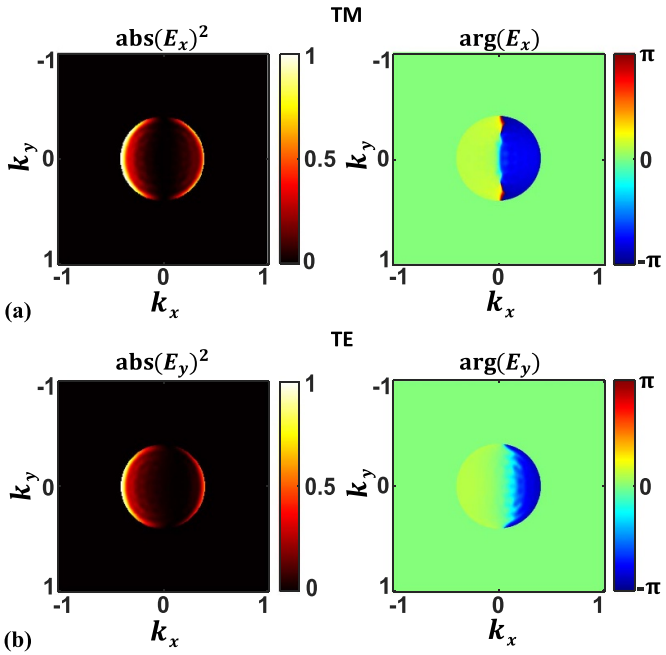

Figure 4. (a) Simulated normalized far-field intensity (on the left) and phase (on the right) for a cliff-like nanostructure with geometrical parameters: swa $= 90^\circ$ and $h = 150$ nm, being illuminated by a TM polarized focused spot having $\lambda = 633$ nm. (b) Corresponding far-field intensity (on the left) and phase (on the right) for the same nanostructure illuminated by a TE polarized focused spot having $\lambda = 633$ nm.

For the study, we have used rigorous 3D FDTD simulations as already discussed. In figure 4(a) we have shown the normalized far-field intensity pattern (on the left) and the corresponding wrapped phase (on the right) for the TM polarized incident beam. Similarly, in figure 4(b) we have shown the normalized far-field intensity pattern (on the left) and the corresponding wrapped phase (on the right) for the TE polarized incident beam. Here, we observe two asymmetric radiation fields along the $x-$axis i.e. along the direction of variation in the nanostructure profile, with the central region of the far-field experiencing weak radiation because of the interference of the beam that is scattered by the two halves of the nanostructure [7]. Further, we observe a phase jump along the nanostructure induced by the height variation (which produces the phase variation) of the nanostructure. While the far-field intensity patterns appear similar for both TE and TM polarizations, there are variations in the intensities of the two asymmetric peaks. This discrepancy arises as a consequence of the distinct treatment of TE and TM polarized beams due to the electromagnetic boundary conditions, i.e. the continuity in both tangential components and their derivatives of the electric fields [42].

We introduce the concept of 'visibility' (V) as a quantitative parameter that characterizes the relative contrast between the two distinct radiation fields observed in the far-field intensity pattern. The V is a parameter that depends on the swa and the height of the nanostructure. As the geometrical parameters of the nanostructure are varying the V will vary providing us with a unique means for calibration. A similar calibration of nanoparticle size has been performed by Kolenov and Pereira [43]. In figure 5, we illustrate the procedure for calculating V applicable to any normalized far-field intensity pattern of a cliff-shaped nanostructure. Initially, we examine the cross-section along the $k_y = 0$ plane within the normalized far-field intensity pattern. Subsequently, we designate the two radiation peaks as pk_1 (the peak corresponding to $-k_x$) and pk_2 (the peak corresponding to $+k_x$). Finally, the parameter V is quantitatively determined through the following mathematical expression:

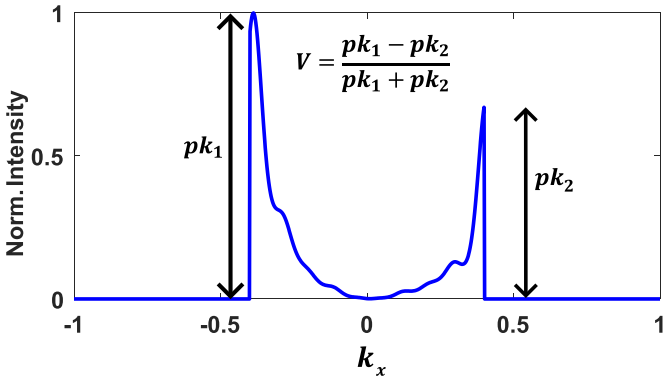

Figure 5. Schematic describing the quantity visibility (V) parameter.

$$V = \frac{pk_1 - pk_2}{pk_1 + pk_2}. \tag{4}$$

This quantitative parameter V allows us the further possibility to optimize the experimental setup, where instead of utilizing a CCD camera we can replace it with a set of single-pixel detectors positioned along the k_x-axis which measures pk_1 and pk_2 separately while yielding the quantity V. This in turn will reduce the noises associated with the CCD camera, further reducing the computation associated with quantifying V from a far-field intensity map.

3.2. *Numerical calibration of CFS for steep* swa *and height*

In this section, we investigate the influence of the two geometrical parameters, namely the steep swa and the height (h), on the far-field intensity patterns exhibited by the cliff-like nanostructure when subjected to illumination from a linearly polarized focused beam. Our investigation encompasses two distinct aspects: the impact of variation in swa and the impact of variation in h, each considered independently. To explore these effects comprehensively, we systematically vary the swa over a range spanning 70° to 100° while varying h within the range of 100 nm to 300 nm for separate analyses.

Let us first explore the effects of swa on the far-field intensity pattern of the cliff-like nanostructure. In figure 6(a) we have shown the normalized far-field intensity pattern cross-section in $y = 0$ plane, for cliff-like nanostructure with varying swa$(= 70^\circ$(green curve), 80°(amber curve), and 90°(red curve)) while maintaining a constant $h(= 150$ nm), for a TM polarized incident illuminating beam. Here, we observe that there

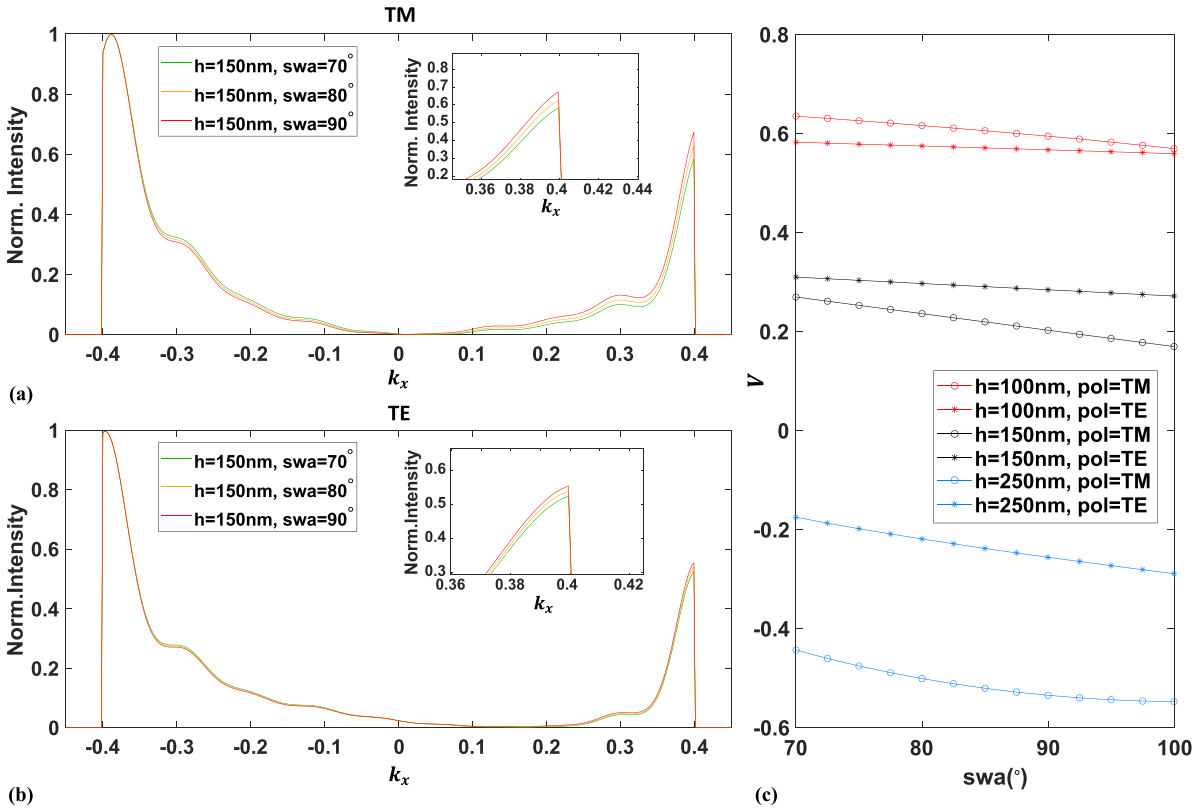

Figure 6. (a) Normalized $k_y = 0$ plane plotted for three different cliff-like nanostructures with different swa($= 70°, 80°$, and $90°$) but fixed $h(= 150$ nm), when illuminated by TM polarized beam. (b) Normalized $k_y = 0$ plane plotted for three different cliff-like nanostructures with different swa($= 70°, 80°$, and $90°$) but fixed $h(= 150$ nm), when illuminated by TE polarized beam. (c) Calibration curves of swa are shown for three different $h(= 100$ nm, 150 nm, and 250 nm) for TE and TM polarized incident illumination schemes.

is a significant difference in the value $pk_1 - pk_2$ for the different swa, resulting in different values of V. Consequently, in figure 6(b) we have shown the analogous cross-sections for the same cliff-like nanostructure parameters but under TE polarized incident illumination. Although differences in $pk_1 - pk_2$ persist across varying swa, the differences are comparatively smaller than those observed in the TM polarized scenario. This implies that TM polarization exhibits greater sensitivity to alterations in swa than its TE counterpart. Further, we perform a comprehensive study to understand the trend of change due to the impact of swa by sweeping it in the range spanning $70°$ to $100°$, with the parameter V calculated for three different heights ($h = 100$ nm (red curve), 150 nm (black curve), and 250 nm (blue curve)) as shown in figure 6(c). Notably, asterisk-marked curves signify TE polarization, while curves marked with circles represent TM polarization. We observe that for the different heights, TM polarization is more sensitive to changes in the swa. This sensitivity is further accentuated with increasing height, attributing this trend to the increased lateral shadow accompanying the growth of the nanostructure's height.

Now, let us investigate the effects of varying h on the far-field intensity pattern of the cliff-like nanostructure. In this context, altering h introduces a corresponding modification in the phase difference between the scattered fields emanating from distinct height levels within the structure, resulting in variation in the far-field intensities. For the scenario where $h = \lambda/4$ and swa $= 90°$, a phase shift of π is introduced, resulting in destructive interference between the scattered beams emanating from different regions within the structure. Similarly, when $h = \lambda/2$ and swa $= 90°$, a phase shift of 2π leads to constructive interference, rendering the change in h inconspicuous to the incident beam. As we vary the h, deviations from these distinctive cases become apparent. In figure 7(a) we have shown the normalized far-field intensity pattern cross-section in $y = 0$ plane, for cliff-like nanostructure with varying $h(= 100$ nm (green curve), 150 nm (amber curve), and 225 nm(red curve)) while maintaining a constant swa$(= 80°)$, for a TM polarized incident illuminating beam. Here, we observe that there is a more pronounced difference in the value $pk_1 - pk_2$ for the different h compared to the variations induced by changing swa. An intriguing observation emerges at $h = 225$ nm where the far-field seems to flip i.e. $pk_1 < pk_2$, this is due to the fact that at this h we have a phase difference surpassing π. Consequently, in figure 7(b) we have shown the analogous cross-sections for the same cliff-like nanostructure parameters but under TE polarized incident illumination. Here, we observe that the difference in the value $pk_1 - pk_2$ is comparably substantial for both TE and TM polarizations, suggesting that the variation in h is sensitive for both the polarizations states. Further, we perform a comprehensive study to understand the trend of change due to the impact of h by sweeping it in the range spanning 100 nm to 300 nm, with

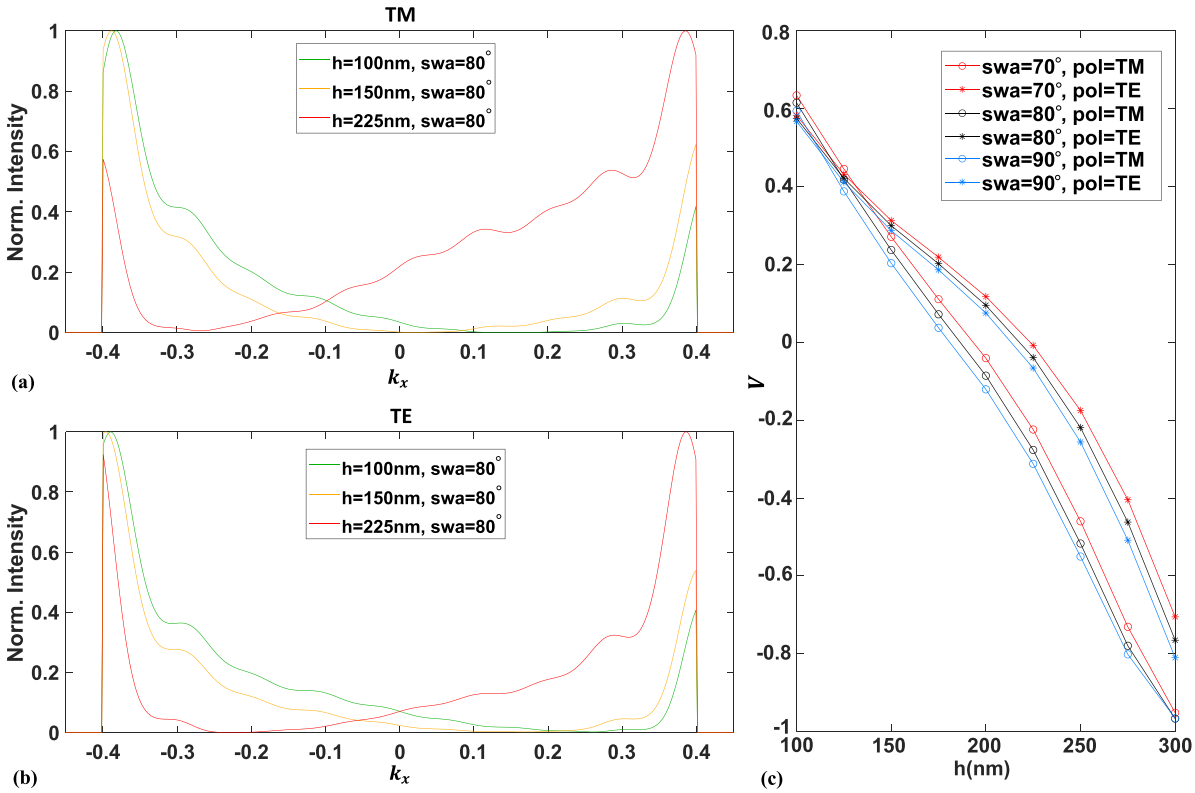

Figure 7. (a) Normalized $k_y = 0$ plane plotted for three different cliff-like nanostructures with different $h(= 100\,\text{nm}, 150\,\text{nm}, \text{and } 225\,\text{nm})$ but fixed swa$(= 80°)$, when illuminated by TM polarized beam. (b) Normalized $k_y = 0$ plane plotted for three different cliff-like nanostructures with different $h(= 100\,\text{nm}, 150\,\text{nm}, \text{and } 225\,\text{nm})$ but fixed swa$(= 80°)$, when illuminated by TE polarized beam. (c) Calibration curves of h are shown for three different swa$(= 70°, 80°, \text{and } 90°)$ for TE and TM polarized incident illumination schemes.

the parameter V calculated for three different swa$(= 70°$(red curve$), 80°$(black curve$)$, and $90°$(blue curve$)$) as shown in figure 7(c). The curves marked with asterisks denote TE polarization, while circles represent TM polarization. The quasi-periodic curves as shown in figure 7(c) stem from the interplay between the phase difference introduced by the cliff-like nanostructure among different segments of the incident beam. These findings demonstrate the capability of CFS as an adept calibration tool for precisely gauging nanostructures characterized by steep swa and varying heights (h).

3.3. Sensitivity analysis of CFS

In this section, we analyze the sensitivity of the proposed CFS method for the calibration of steep swa against the edge roundness of the cliff-like nanostructure; and the variation in the position of the cliff-like nanostructure with respect to the focused beam.

Accordingly, for the analysis of the influence of edge roundness of the cliff-like nanostructure, we introduce roundness $r(= 0\,\text{nm}$ to $10\,\text{nm})$ to the nanostructure (as shown in figure 8), for one such nanostructure with parameters: swa $= 90°$ and $h = 100\,\text{nm}$. We measure the deviation introduced in V due to the roundness in the cliff-like nanostructure, by calculating ΔV, where $\Delta V = |V_r - V_{r=0}|$. Here, the subscript r denotes the roundness in the cliff-like nanostructure. In figure 8(a) we have shown the deviation introduced in V due

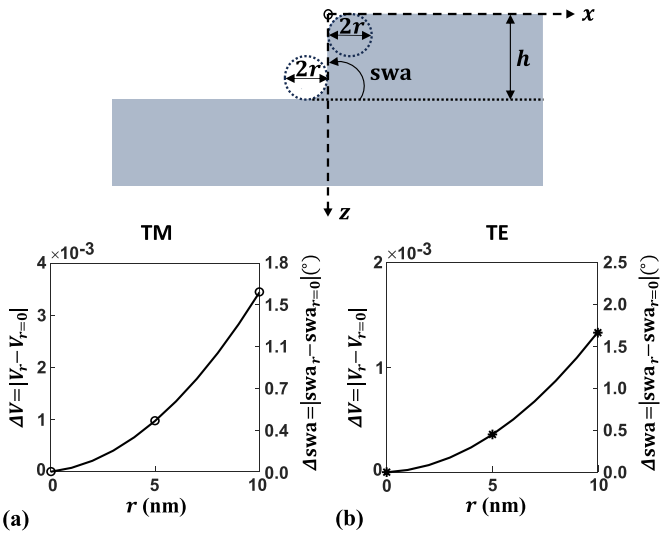

Figure 8. Sensitivity analysis, indicating edge roundness of 10 nm in nanostructure results in a swa variation within 1.7°.

to the roundness in the cliff-like nanostructure for TM polarized incident beam. Similarly, in figure 8(b) we have shown the deviation introduced in V due to the roundness in the cliff-like nanostructure for TE polarized incident beam. The resulting deviation in the swa measurement, denoted by Δswa, where $\Delta\text{swa} = |\text{swa}_r - \text{swa}_{r=0}|$ is represented in the vertical right

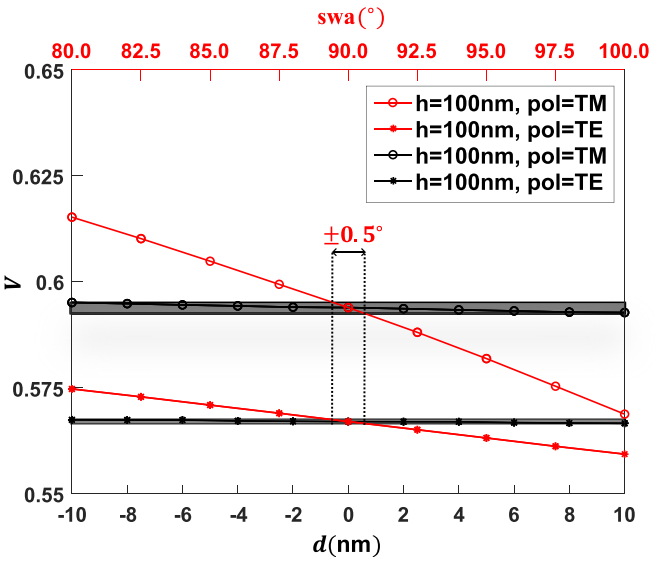

Figure 9. Sensitivity analysis, indicating fluctuation of ±10 nm in position of nanostructure results in a stable swa within the range of ±0.5°.

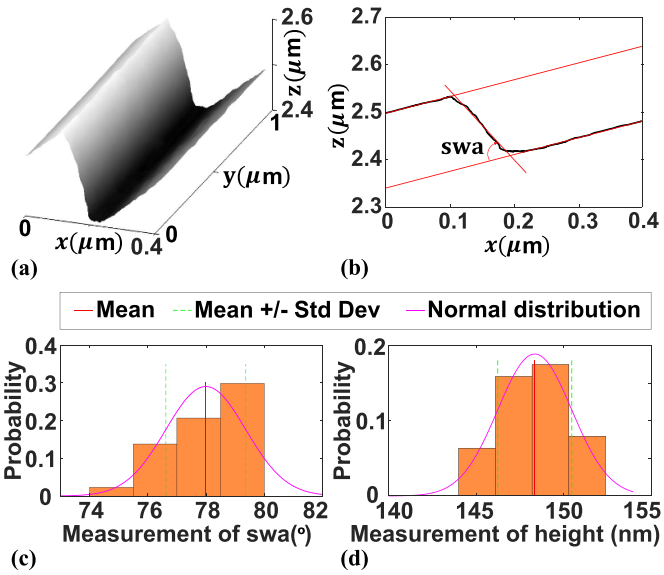

Figure 10. (a) 3D visualization of the tilted-AFM data. (b) A cross-section of the AFM data (shown in (a)), where we define the swa of the profile. (c) Histogram representing the variation in swa in the AFM measurement. (d) Histogram representing the variation in height (h) in the AFM measurement.

axis for both plots. We observe that V varies exponentially with the edge roundness, although for edge roundness within 10 nm the resulting variation of swa is within 1.7° for both the polarization states. Such a variation of V around the edge roundness of the nanostructure confirms the robustness of the proposed CFS method implemented against unwanted roundness on the edge of the nanostructure. Further for nanostructures with larger h, the deviation in swa due to the same extent of roundness (i.e. $r = 10$ nm) will be less than 1.7°. This is due to the fact that the effective variation in the nanostructure reduces as the h increases for the same roundness. We also note that for high values of roundness, the proposed method will not be sensitive; this is understandable because as the quality of the nanostructure reduces, the definition of swa cannot be that of the ideal nanostructure.

Now, we analyze the sensitivity of the proposed CFS method for the calibration of steep swa against variation in the position of the cliff-like nanostructure with respect to the focused beam. For that, we introduce a displacement $d(= -10$ nm to $+10$ nm) to the nanostructure with respect to the position $b = 0$, for one such nanostructure with parameters: swa = 90° and $h = 100$ nm. In figure 9 we have shown the variation in V due to the displacement in the nanostructure position with respect to the focused beam in the horizontal bottom axis (shown in black curves), together with the swa calibration curve of the nanostructure (as shown in figure 6(c)) in the horizontal top axis (shown in red curves). The curves marked with asterisks denote TE polarization, while circles represent TM polarization. We observe that V remains unaltered even in the presence of sufficient fluctuations in the position of the nanostructure, resulting in a variation of swa within the range of ±0.5°. Here, we observe that the proposed method has a stable value for V as long as the variation in the position of the nanostructure is within 20 nm with respect to the focused beam. Such a stable value of V around the displacement in the position of the nanostructure confirms the robustness of the proposed CFS method implemented against unwanted fluctuations due to tolerances of the piezo translation stage used in the experiments.

3.4. Experimental verification

In this section, we demonstrate the experimental verification of our numerically simulated results. For that, we measure a cliff-like nanostructure made up of material Si. Further, to establish the ground truth of the geometrical parameters of the nanostructure, the height h and swa have been independently measured by an AFM. In order to determine the steep swa value, we mounted the sample in a holder with a tilt of 60° and analyzed the measurements following Dai *et al* [44]. In figure 10(a) we have shown the 3D visualization of the tilted-AFM measurement data. Consequently, in figure 10(b) we have shown a cross-section profile of the data (shown in black curve), where we measure the steep swa by fitting straight lines through the edge of the profile (shown in red curves) and calculating the angles between them. From the AFM data, we obtain that the geometrical parameters of the nanostructure are: swa = 77.99° ± 1.37° and $h = 148.35$ nm ±2.11 nm. In figures 10(c) and (d) we have shown the histograms representing the variation in measurement of swa and height of the cliff-like nanostructure, respectively.

Now, to perform experimental measurements using CFS, we have used the setup as depicted in figure 2. Here, we illuminate the cliff-like nanostructure using a TE or TM polarized focused spot using a microscope objective having $NA = 0.4$. The cliff-like nanostructure sample is placed on the piezo

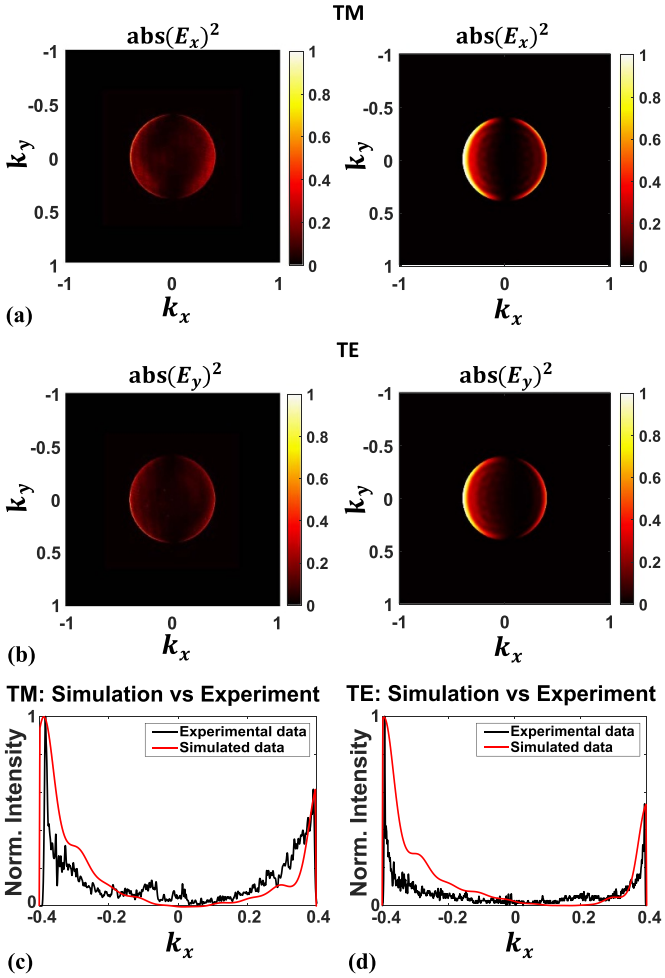

Figure 11. (a) Experimental and simulated normalized far-field for TM polarized incident beam. (b) Experimental and simulated normalized far-field for TE polarized incident beam. (c) Cross-section along $k_y = 0$ plane of results shown in (a). (d) Cross-section along $k_y = 0$ plane of results shown in (b).

translation stage, which is used to position the sample at the center of the optical axis of the focused beam. Finally, the scattered field is captured by the CCD camera. In the experiment, we capture a set of five far-field intensity images for each TE and TM polarized incident beam, while moving the sample around the center of the optical axis of the focused beam, this is done because the sample cannot be aligned exactly at the center of the optical axis of the focused beam. In figure 11(a) we have shown the experimentally captured normalized far-field intensity (on the left) and corresponding closest simulated normalized far-field intensity with geometrical parameters: swa $= 77.5°$ and $h = 150$ nm (on the right). The incident illumination beam is TM polarized. Consequently, in figure 11(b) we have shown the analogous normalized far-field intensity for the same cliff-like nanostructure parameters but under TE polarized incident illumination. Here, we observe that while exact matching between simulated and experimental far-fields was not achieved due to inherent simulation limitations and the noise in the setup, both the experimental and simulated far-fields exhibit significant agreement with each other. To further validate this concordance, in figure 11(c) we have plotted the cross-section along $k_y = 0$ the plane for both experimental (black curve) and simulated (red curve) far-field intensities for TM polarized incident illumination. Similarly, in figure 11(d) we have plotted the cross-section along the $k_y = 0$ plane for both experimental (black curve) and simulated (red curve) far-field intensities for TE polarized incident illumination. Here, we have used a moving average low pass filter on the cross-sections to reduce the high-frequency noise. We observe that pk_1 and pk_2 match for both TE and TM polarization states for both experiments as well as simulations. Further, for the experimentally measured far-field intensities, the parameter V yields the value 0.241 ± 0.012 for TM polarized incident illumination and 0.299 ± 0.005 for TE polarized incident illumination. We introduce a customized figure of Merit (FOM), analogous to the reduced χ^2 [45], defined as the FOM$_{\chi^2}$. The FOM$_{\chi^2}$ can be calculated with, $\text{FOM}_{\chi^2} = [1/n]\sum_i^n [k_{x_i}^{\text{Exp}} - k_{x_i}^{\text{Sim}}]^2/\delta V$, where n is the total number of measurement points, k_x^{Exp} and k_x^{Sim} are the normalized cross-section along $k_y = 0$ plane of the far-field of experiment and simulation, as shown in figures 11(c) and (d), δV is the uncertainty measured in V. In our measurements, we find $\text{FOM}_{\chi^2}^{TM} = 1.85$ and $\text{FOM}\chi^{2^{TE}} = 5.4$. The calibration curve presented in figures 6(c) and 7(c) facilitates the determination of the height and swa value as $h = 149.42$ nm ± 1.66 nm and swa $= 77.75° \pm 3.61°$ from the TM polarization calibration curve and $h = 150.05$ nm ± 1.04 nm and swa $= 78.36° \pm 3.89°$ from the TE polarization calibration curve. The results experimentally demonstrate that CFS is a viable calibration tool for the measurement of the steep swa and heights (h) of cliff-like nanostructures.

4. Discussions and conclusions

In this paper, we have successfully demonstrated the effectiveness of CFS as a robust calibration tool for accurately measuring steep swa and heights of cliff-like nanostructures. Our experimental and simulated results show a reasonable agreement, validating the method's reliability. In this work, we have introduced a 'visibility' parameter that uniquely quantifies the far-field intensity, providing a quantitative means to assess steep swa and heights. Utilizing this parameter, the CFS system can further be optimized by replacing the CCD camera in the setup with a set of single-pixel detectors that perform the arithmetic calculation for 'visibility'. The proposed method indicates a higher sensitivity to the TM polarization state for calibrating steep swa while for calibration of height both the polarization states are equally sensitive. Furthermore, a comprehensive sensitivity analysis reveals the stable nature of our method, showcasing that even with fluctuations of ± 10 nm in the position of the nanostructure, the resulting swa remains stable within a range of $\pm 0.5°$. The exponential variation of the visibility parameter with edge roundness is observed, with fluctuations in edge roundness within 10 nm resulting in swa variations within $1.7°$ for both polarization states. Further, as the variation introduced due to the swa being relatively small this method is prone to stability, noise, and alignment of the

system. Performing experimental calibration could provide an alternative if the system is not ideal. Our analysis revealed that while exact matching between simulated and experimental far-fields was not achieved due to inherent simulation limitations, we observed similar trends in the dependence of far-field behavior on swa, strengthening the confidence in our findings. In our experimental validations, we find a reasonable agreement between the CFS-derived and AFM measurements. The swa ($77.99° \pm 1.37°$) and height (148.35 nm $\pm$2.11 nm) values obtained from AFM closely align with the corresponding swa ($77.75° \pm 3.61°$, $78.36° \pm 3.89°$) and height (149.42 nm $\pm$1.66 nm, 150.05 nm $\pm$1.04 nm) values derived from CFS calibration curves for TM and TE incident beams, respectively. Future research endeavors involve the application of CFS to more complex cliff-like nanostructures, particularly those with layered compositions, where the uncertainties associated with optical constants become increasingly significant. Thin layers within these nanostructures can introduce variations in optical constants depending on their thickness, influencing the overall accuracy of our measurements. Therefore, investigating the influences of simulation errors, including variations in optical constants, on the calibration curves obtained through FDTD-based simulations becomes important for these complex nanostructures. Understanding these influences will be critical for refining our methodology and ensuring its robustness and accuracy across varying experimental conditions and material properties. Additionally, considering the impact of aberrations within the experimental setup and the roughness of the nanostructure sample is essential, as they can significantly affect the measured results. We intend to explore and address these effects to enhance the reliability and accuracy of our experimental measurements in future studies. Additionally, investigating the scalability of the technique to industrial manufacturing processes could pave the way for its integration into commercial nanofabrication workflows. The findings of this study underscore the significance of the CFS technique as a powerful tool for nanostructure characterization. By enabling accurate and reliable measurements of steep swa and heights, CFS contributes to the advancement of nanotechnology and holds promise for a wide range of applications in nanoscale metrology and beyond.

Data availability statement

The data cannot be made publicly available upon publication because they are not available in a format that is sufficiently accessible or reusable by other researchers. The data that support the findings of this study are available upon reasonable request from the authors.

Acknowledgments

We acknowledge the Project 20FUN02 POLight, co-financed by the Participating States and from the European Union's Horizon 2020 research and innovation programme, and Nederlandse Organisatie voor Wetenschappelijk Onderzoek (Project 17-24 Synoptics No. 2) for funding this research. We also would like to thank Rodolf Herfst from TNO for the AFM measurements.

ORCID iDs

Anubhav Paul https://orcid.org/0000-0002-4167-6256
Jila Rafighdoost https://orcid.org/0000-0003-4555-7219
Xiujie Dou https://orcid.org/0000-0002-8135-7890
Silvania F Pereira https://orcid.org/0009-0001-9148-1975

References

[1] Hoefflinger B 2011 ITRS: the international technology roadmap for semiconductors *Chips 2020: A Guide to the Future of Nanoelectronics* (Springer) pp 161–74
[2] Hansen H N, Carneiro K, Haitjema H and De Chiffre L 2006 Dimensional micro and nano metrology *CIRP Ann.* **55** 721–43
[3] Vogel E 2007 Technology and metrology of new electronic materials and devices *Nat. Nanotechnol.* **2** 25–32
[4] Moreau W M 2012 *Semiconductor Lithography: Principles, Practices and Materials* (Springer)
[5] Edwards C, Arbabi A, Popescu G and Goddard L L 2012 Optically monitoring and controlling nanoscale topography during semiconductor etching *Light Sci. Appl.* **1** e30
[6] Kim H W, Lee J Y, Shin J, Woo S G, Cho H K and Moon J T 2004 Experimental investigation of the impact of LWR on sub-100-nm device performance *IEEE Trans. Electron Devices* **51** 1984–8
[7] Dou X, Pereira S F, Min C, Zhang Y, Meng P, Urbach H P and Yuan X 2021 Determination of steep sidewall angle using polarization-sensitive asymmetric scattering *Meas. Sci. Technol.* **32** 085201
[8] Dou X, Min C, Zhang Y, Pereira S F and Yuan X 2022 Optical singularity assisted method for accurate parameter detection of step-shaped nanostructure in coherent Fourier scatterometry *Opt. Express* **30** 29287–94
[9] Cisotto L, Pereira S F and Urbach H P 2018 Analytical calculation on the determination of steep side wall angles from far field measurements *J. Opt.* **20** 065601
[10] Gödecke M, Peterhänsel S, Frenner K and Osten W 2016 Robust determination of asymmetric side wall angles by means of coherent scanning fourier scatterometry *Proc. SPIE* **9890** 150–7
[11] Frase C G, Buhr E and Dirscherl K 2007 CD characterization of nanostructures in SEM metrology *Meas. Sci. Technol.* **18** 510
[12] Fukaya H *et al* 2011 New CD-SEM metrology method for the side wall angle measurement using multiple detectors *Proc. SPIE* **8081** 81–91
[13] Lee S, Lee J, Ban S, Oh H K, Nam B, Kim S, Yim D and Kim O 2013 A technique for the non-destructive EUV mask sidewall angle measurement using scanning electron microscope *J. Nanosci. Nanotechnol.* **13** 8032–5
[14] Xie H, Hussain D, Yang F and Sun L 2014 Atomic force microscopy deep trench and sidewall imaging with an optical fiber probe *Rev. Sci. Instrum.* **85** 123704
[15] Ju B F, Chen Y L, Zhang W and Fang F 2012 Rapid measurement of a high step microstructure with 90° steep sidewall *Rev. Sci. Instrum.* **83** 013706
[16] Hussain D, Ahmad K, Song J and Xie H 2016 Advances in the atomic force microscopy for critical dimension metrology *Meas. Sci. Technol.* **28** 012001
[17] Yacoot A and Koenders L 2008 Aspects of scanning force microscope probes and their effects on dimensional measurement *J. Phys. D: Appl. Phys.* **41** 103001

[18] Kizu R, Misumi I, Hirai A, Kinoshita K and Gonda S 2018 Development of a metrological atomic force microscope with a tip-tilting mechanism for 3D nanometrology *Meas. Sci. Technol.* **29** 075005

[19] Hermosa N, Rosales-Guzmán C, Pereira S F and Torres J P 2014 Nanostep height measurement via spatial mode projection *Opt. Lett.* **39** 299–302

[20] Ortega-Arroyo J and Kukura P 2012 Interferometric scattering microscopy (iSCAT): new frontiers in ultrafast and ultrasensitive optical microscopy *Phys. Chem. Chem. Phys.* **14** 15625–36

[21] Rodríguez-Fajardo V and Forbes A 2022 Measurement of nanometric heights by modal decomposition *Phys. Rev. Appl.* **18** 064068

[22] Trueb J T, Avci O, Sevenler D, Connor J H and Ünlü M S 2016 Robust visualization and discrimination of nanoparticles by interferometric imaging *IEEE J. Sel. Top. Quantum Electron.* **23** 394–403

[23] Abbe E 1873 Beiträge zur theorie des mikroskops und der mikroskopischen wahrnehmung *Arch. Mikr. Anat.* **9** 413–68

[24] Madsen M H and Hansen P E 2016 Scatterometry-fast and robust measurements of nano-textured surfaces *Surf. Topography: Metrol. Prop.* **4** 023003

[25] Orji N G, Badaroglu M, Barnes B M, Beitia C, Bunday B D, Celano U, Kline R J, Neisser M, Obeng Y and Vladar A 2018 Metrology for the next generation of semiconductor devices *Nat. Electron.* **1** 532–47

[26] Huang H T, Kong W and Terry J F L 2001 Normal-incidence spectroscopic ellipsometry for critical dimension monitoring *Appl. Phys. Lett.* **78** 3983–5

[27] Gödecke M L, Frenner K and Osten W 2021 Model-based characterisation of complex periodic nanostructures by white-light Mueller-matrix Fourier scatterometry *Light Adv. Manuf.* **2** 237–50

[28] Ferreras Paz V, Peterhänsel S, Frenner K and Osten W 2012 Solving the inverse grating problem by white light interference Fourier scatterometry *Light Sci. Appl.* **1** e36–e36

[29] Kline R J, Sunday D F, Windover D and Bunday B D 2017 x-ray scattering critical dimensional metrology using a compact x-ray source for next generation semiconductor devices *J. Micro Nanolithography MEMS MOEMS* **16** 014001

[30] Roy S, Bouwens M, Wei L, Pereira S F, Urbach H P and Van Der Walle P 2015 High speed low power optical detection of sub-wavelength scatterer *Rev. Sci. Instrum.* **86** 123111

[31] Roy S, Assafrao A, Pereira S F and Urbach H P 2014 Coherent Fourier scatterometry for detection of nanometer-sized particles on a planar substrate surface *Opt. Express* **22** 13250–62

[32] Kumar N, El Gawhary O, Roy S, Pereira S F and Urbach H P 2013 Phase retrieval between overlapping orders in coherent Fourier scatterometry using scanning *J. Eur. Opt. Soc. Rapid Publ.* **8** 13048

[33] Kumar N, Petrik P, Ramanandan G K, El Gawhary O, Roy S, Pereira S F, Coene W M and Urbach H P 2014 Reconstruction of sub-wavelength features and nano-positioning of gratings using coherent Fourier scatterometry *Opt. Express* **22** 24678–88

[34] Gödecke M, Peterhänsel S, Buchta D, Frenner K and Osten W 2017 Detection of grating asymmetries by phase-structured illumination *Fifth Int. Conf. on Optical and Photonics Engineering* vol 10449 (SPIE) pp 61–68

[35] Paul A, Kolenov D, Scholte T and Pereira S F 2023 Coherent Fourier scatterometry: a holistic tool for inspection of isolated particles or defects on gratings *Appl. Opt.* **62** 7589–95

[36] Kolenov D, Zadeh I E, Horsten R C and Pereira S F 2021 Direct detection of polystyrene equivalent nanoparticles with a diameter of 21 nm ($\sim\lambda/19$) using coherent Fourier scatterometry *Opt. Express* **29** 16487–505

[37] Stamnes J J 2017 *Waves in Focal Regions: Propagation, Diffraction and Focusing of Light, Sound and Water Waves* (Routledge)

[38] Stratton J A 2007 *Electromagnetic Theory* vol 33 (Wiley)

[39] Ansys Lumerical FDTD solutions (available at: www.lumerical.com/)

[40] Richards B and Wolf E 1959 Electromagnetic diffraction in optical systems, II. Structure of the image field in an aplanatic system *Proc. R. Soc.* A **253** 358–79

[41] Novotny L and Hecht B 2012 *Principles of Nano-Optics* (Cambridge University Press)

[42] Qu D, Yuan X and Burge R 1993 Polarization dependence of the electromagnetic field distribution across wavelength-sized relief grating surfaces *J. Opt. Soc. Am.* A **10** 2317–23

[43] Kolenov D and Pereira S F 2020 Machine learning techniques applied for the detection of nanoparticles on surfaces using coherent Fourier scatterometry *Opt. Express* **28** 19163–86

[44] Dai G, Hahm K, Scholze F, Henn M A, Gross H, Fluegge J and Bosse H 2014 Measurements of CD and sidewall profile of EUV photomask structures using CD-AFM and tilting-AFM *Meas. Sci. Technol.* **25** 044002

[45] Jellison J G E 1993 Data analysis for spectroscopic ellipsometry *Thin Solid Films* **234** 416–22